

Securing SIM-Assisted Wireless Networks via Quantum Reinforcement Learning

Le-Hung Hoang, Quang-Trung Luu, Dinh Thai Hoang, Diep N. Nguyen, and Van-Dinh Nguyen

Abstract—Stacked intelligent metasurfaces (SIMs) have recently emerged as a powerful wave-domain technology that enables multi-stage manipulation of electromagnetic signals through multilayer programmable architectures. While SIMs offer unprecedented degrees of freedom for enhancing physical-layer security, their extremely large number of meta-atoms leads to a high-dimensional and strongly coupled optimization space, making conventional design approaches inefficient and difficult to scale. Moreover, existing deep reinforcement learning (DRL) techniques suffer from slow convergence and performance degradation in dynamic wireless environments with imperfect knowledge of passive eavesdroppers. To overcome these challenges, we propose a hybrid quantum proximal policy optimization (Q-PPO) framework for SIM-assisted secure communications, which jointly optimizes transmit power allocation and SIM phase shifts to maximize the average secrecy rate under power and quality-of-service constraints. Specifically, a parameterized quantum circuit is embedded into the actor network, forming a hybrid classical-quantum policy architecture that enhances policy representation capability and exploration efficiency in high-dimensional continuous action spaces. Extensive simulations demonstrate that the proposed Q-PPO scheme consistently outperforms DRL baselines, achieving approximately 15% higher secrecy rates and 30% faster convergence under imperfect eavesdropper channel state information. These results establish Q-PPO as a powerful optimization paradigm for SIM-enabled secure wireless networks.

Index Terms—Stacked intelligent metasurfaces, quantum reinforcement learning, physical layer security, and reconfigurable intelligent surface.

I. INTRODUCTION

THE sixth-generation (6G) networks are expected to revolutionize wireless communications by delivering significant improvements over 5G in terms of data throughput, energy efficiency, and massive connectivity [2]. However, the explosive growth of connected devices, together with the broadcast nature of wireless channels, substantially increases the risk of confidential data leakage to unauthorized receivers. As a result, emerging 6G applications demand not only ultra-low latency and high-precision localization but also stringent security guarantees, thereby imposing more rigorous require-

Part of this work was presented at the IEEE International Conference on Advanced Technologies for Communications, Oct. 2025, Hanoi, Vietnam [1].

L.-H. Hoang is with the Smart Green Transformation Center, VinUniversity, Vinhomes Ocean Park, Hanoi 100000, Vietnam (e-mail: hung.hl@vinuni.edu.vn).

Q.-T. Luu is with Université Paris-Saclay - CNRS - CentraleSupélec - L2S, Gif-sur-Yvette, F-91192, France (e-mail: quangtrung.luu@centralesupelec.fr)

D. T. Hoang and D. N. Nguyen are with the School of Electrical and Data Engineering, University of Technology Sydney, Sydney, NSW 2007, Australia (e-mails: {hoang.dinh, diep.nguyen}@uts.edu.au)

V.-D. Nguyen is with the School of Computer Science and Statistics, Trinity College Dublin, The University of Dublin, Dublin 2, D02 PN40, Ireland (e-mail: dinh.nguyen@tcd.ie).

ments on information privacy protection.

To meet these security requirements, physical-layer security (PLS) has emerged as a promising complementary paradigm for safeguarding wireless communications [3]–[5]. Unlike conventional cryptographic approaches that rely on key distribution and encryption overhead, PLS exploits the intrinsic randomness of wireless channels to enhance confidentiality directly at the physical layer. A variety of PLS techniques have been widely investigated. For instance, artificial noise generation [6] deliberately injects interference to degrade the eavesdropper’s channel while preserving the legitimate link, whereas secure beamforming (e.g., [7] and [8]) steers transmission energy toward intended receivers to suppress information leakage. Despite their effectiveness, these approaches often require additional transmit power, cooperative nodes, or complex hardware architectures, and may fail to guarantee secure communication in certain network configurations.

Driven by the need for more energy-efficient and flexible security solutions, reconfigurable intelligent surfaces (RISs) have recently attracted considerable attention. By adaptively controlling the amplitude and/or phase of incident electromagnetic (EM) waves, RISs enable passive manipulation of the wireless propagation environment, providing finer control than conventional active beamforming [9]–[11]. However, most existing RIS-assisted secure transmission schemes rely on single-layer metasurface architectures [9]–[12]. This structural simplicity inherently limits the available degrees of freedom for wavefront shaping and makes such systems less effective in suppressing multiuser interference, thereby still necessitating complex digital beamforming at the transceiver side [13].

To overcome these limitations, stacked intelligent metasurfaces (SIMs) have recently been proposed as a powerful alternative [14]–[17]. Inspired by artificial neural network architectures, SIMs consist of multiple cascaded metasurface layers that enable fine-grained, multi-stage control of EM wave propagation. By flexibly adjusting the phase shifts of meta-atoms across layers, SIMs can transform the input carrier signal into a desired output waveform, facilitating highly precise beamforming [17], [18]. From a PLS perspective, the multi-layer structure of SIMs provides substantially more degrees of freedom for shaping the propagation environment, allowing the transmitted wavefront to be optimized to strengthen legitimate links while deliberately degrading eavesdropping channels [19]–[21]. Compared with conventional single-layer RIS designs, SIMs enable multiple cascaded transformations, which significantly enhance interference suppression and reduce hardware costs in multiuser beamforming scenarios without requiring large antenna arrays or numerous radio frequency

(RF) chains [15], [16]. These advantages position SIMs as a promising enabler for next-generation physical-layer security solutions.

A. Related Works

Existing studies on SIM-enabled wireless communication systems primarily focus on wave-domain beamforming design [14]–[16], [22], [23]. The SIM concept was first introduced in [22] for multi-user multiple-input single-output (MISO) downlink systems, where joint optimization of transmit power allocation and SIM phase shifts was employed to maximize the sum rate. Simulation results demonstrated that SIM can significantly improve the performance of conventional MISO systems while reducing precoding latency. Subsequently, [14] extended this framework by enabling independent phase control of individual meta-atoms, allowing more flexible wave manipulation across SIM layers. In [23], SIMs were further deployed at both the transmitter and receiver of point-to-point multiple-input multiple-output systems, facilitating direct coding and combining in the EM domain.

Beyond beamforming, SIMs have also been explored as wave-domain information processing platforms. For instance, SIM-assisted channel estimation has been investigated in [24], [25]. Specifically, [24] addressed the underdetermined channel estimation problem by exploiting multiple pilot observations and proposing a reduced-subspace least-squares estimator that leverages the rank deficiency of spatial correlation matrices. Hybrid digital-wave domain estimation strategies were developed in [25] to minimize mean square error, achieving performance comparable to fully digital architectures even with limited RF chains. Moreover, SIMs have recently been utilized as semantic encoders in the wave domain [26], [27]. The work in [26] demonstrated that SIM can map input images into class-dependent beam patterns for low-complexity semantic detection, while [27] showed that a three-layer SIM can perform high-accuracy object classification by transforming semantic features into spectral power distributions. Notably, these studies did not consider secure transmission or the presence of eavesdroppers.

More recently, SIMs have been introduced into PLS design [19]–[21]. In [19], [20], SIM-based anti-eavesdropping strategies were proposed for single-input single-output systems, where SIM simultaneously performs modulation, beamforming, and artificial noise generation to enhance secrecy and energy efficiency. The work in [21] investigated sum secrecy rate maximization for SIM-assisted multi-user MISO systems under transmit power constraints, and developed an alternating optimization framework based on successive convex approximation and projected gradient ascent to handle the non-convexity introduced by discrete SIM phase shifts. While these studies demonstrated the significant secrecy gains achievable with SIM, they relied on the idealized assumption of perfect eavesdropper channel state information (CSI), which is difficult to obtain in practical wireless systems.

Furthermore, most existing SIM optimization frameworks adopt one-shot model-based optimization, resulting in highly coupled and non-convex problems that must be repeatedly solved at each time slot, leading to high computational com-

plexity and sensitivity to initialization [18]. To overcome these limitations, deep reinforcement learning (DRL) has recently emerged as a promising alternative for adaptive SIM control in dynamic wireless environments [8], [28]. By learning policies directly through interaction with the environment, DRL-based schemes can adapt to time-varying channels without requiring complete system knowledge. For example, [29] employed a deep deterministic policy gradient (DDPG) algorithm for joint SIM phase-shift and transmit power optimization, demonstrating superior sum-rate performance compared to conventional optimization methods [30]. However, classical DRL approaches often suffer from slow convergence and scalability issues in high-dimensional SIM control problems, motivating the need for more efficient learning paradigms.

B. Motivations and Main Contributions

Despite the promising secrecy gains offered by intelligent metasurfaces, practical deployment of SIM-enhanced PLS remains severely hindered by high-dimensional control complexity. The multilayer SIM architecture introduces a massive configuration space, leading to a highly coupled and dynamic control problem for real-time phase-shift adaptation in time-varying wireless environments. This dimensional explosion fundamentally challenges the scalability of existing DRL approaches. Conventional DRL methods typically rely on large-scale neural networks (NNs) to approximate high-dimensional policies, which results in slow convergence, prohibitive training times, and excessive computational overhead [31]. These limitations highlight the urgent need for more efficient and scalable learning frameworks for SIM-enabled secure communications.

Recent advances in quantum computing have opened the door to a new class of learning paradigms, quantum reinforcement learning (QRL), which offers a fundamentally different mechanism for addressing high-dimensional control problems. By exploiting quantum superposition and entanglement, QRL enables the simultaneous representation and evaluation of multiple state-action pairs within compact quantum states, thereby significantly enhancing exploration efficiency and accelerating convergence [32]. Moreover, quantum entanglement preserves intrinsic correlations across the state-action space, allowing learning updates in one region to propagate globally and reducing the number of samples required to approach optimal policies [33], [34]. These properties make QRL particularly well-suited for large-scale SIM configuration tasks.

Motivated by these observations, this paper proposes the first hybrid QRL framework for SIM-assisted PLS under imperfect eavesdropper CSI. We investigate a SIM-enhanced multi-user MISO downlink system and develop a quantum proximal policy optimization (Q-PPO) algorithm that jointly optimizes transmit power allocation and SIM phase shifts to maximize the long-term average secrecy rate (ASR). The main contributions of this paper are summarized as follows:

- We investigate a SIM-assisted multi-user MISO downlink system in the presence of a passive eavesdropper with imperfect CSI. Unlike most existing SIM security studies that assume perfect knowledge of the eavesdropper's channel, we explicitly model CSI uncertainty and for-

mulate a long-term average secrecy-rate maximization problem by jointly optimizing transmit power allocation and SIM phase-shift configurations under power and quality-of-service (QoS) constraints. This provides a more realistic and practically relevant design framework for SIM-enabled PLS.

- We propose a hybrid quantum-classical PPO algorithm, termed Q-PPO, to address the extremely high-dimensional and strongly coupled SIM control problem. By embedding parameterized quantum circuits (PQCs) into the actor network [35], Q-PPO exploits quantum superposition and entanglement to represent and explore large continuous action spaces more efficiently than classical DRL. This architecture significantly improves exploration efficiency, accelerates convergence, and reduces the reliance on large classical neural networks when learning SIM phase-shift and power allocation policies.
- Through extensive simulations, we demonstrate that Q-PPO consistently outperforms state-of-the-art (SOTA) DRL methods such as PPO, DDPG, and twin delayed DDPG (TD3) as well as existing SIM approaches [29], [30] in terms of ASR, convergence speed, and robustness to eavesdropper CSI uncertainty. We further provide quantitative insights into how the number of qubits and the depth of the quantum circuit affect learning efficiency and secrecy performance, and show that SIM architectures themselves offer substantial secrecy gains under dynamic and uncertain wireless conditions.

The remainder of this paper is organized as follows. Section II describes the system model, formulates the secrecy-rate maximization problem, and reviews the Markov decision process (MDP) framework used to characterize the system dynamics and uncertainties. Section III presents the fundamentals of RL and details the proposed Q-PPO algorithm. Section IV reports numerical results and analyzes the performance under various scenarios. Finally, Section V concludes the paper.

II. SYSTEM MODEL AND PROBLEM FORMULATION

As illustrated in Fig. 1, we consider the downlink transmission of a secure MISO communication system. The system consists of a base station (BS) equipped with a SIM to enhance communication performance from K antennas to the set $\mathcal{M} \triangleq \{1, \dots, M\}$ of M single-antenna communication users (CUs). In addition to the legitimate users, we assume the presence of a passive eavesdropper (Eve) attempting to intercept confidential messages intended for any CU $m \in \mathcal{M}$.

A. SIM Model

The SIM is modeled as a closed vacuum container composed of multiple stacked metasurface layers [36]. Each metasurface layer contains a large number of meta-atoms [37], which are connected to a smart controller, *e.g.*, a field programmable gate array board. By appropriately configuring the complex-valued transmission coefficients of the meta-atoms in each layer, their EM responses, specifically amplitude and phase shift, can be independently adjusted. Through this configuration, the SIM is capable of performing downlink beamforming directly in

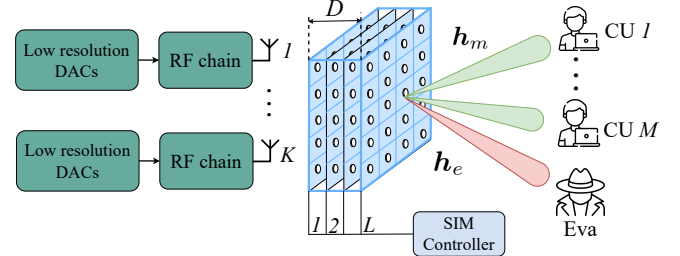


Fig. 1: The SIM-aided secure multi-user communication system model.

the wave domain [22].

Let $\mathcal{L} \triangleq \{1, \dots, L\}$ denote the set of metasurface layers, and $\mathcal{N}_l \triangleq \{1, \dots, N\}$ represent the set of meta-atoms within layer $l \in \mathcal{L}$. Note that, in this paper, we consider square metasurface arrays, *i.e.* $N = n_{\max}^2$, with $n_{\max} \in \mathbb{N}$. We define θ_n^l as the phase shift of meta-atom n on layer l , which can be continuously adjusted in the range $[0, 2\pi]$. Accordingly, the diagonal phase shift matrix of the metasurface layer l is defined as:

$$\Phi^l = \text{diag} \left(e^{j\theta_1^l}, \dots, e^{j\theta_N^l} \right) \in \mathbb{C}^{N \times N}, \quad \forall l \in \mathcal{L} \quad (1)$$

where $e^{j\theta_n^l}$ denotes the transmission coefficient imposed by meta-atom n on metasurface layer l . Similar to [23], we consider metasurfaces as uniform planar arrays. Specifically, as shown in Fig. 1, the metasurfaces rely on an isomorphic lattice arrangement, and are parallel to the xz -plane. The distance between two different meta-atoms (n and n') on the metasurface can be expressed as

$$d_{n,n'} = d_a \sqrt{(n_x - n'_x)^2 + (n_z - n'_z)^2} \quad (2)$$

where d_a denotes the distance between adjacent meta-atoms on a metasurface. Additionally, n_x and n_z denote the indices of meta-atom n along the x -axis and the z -axis, respectively, which are defined as

$$n_x = \text{mod}(n - 1, n_{\max}) + 1; \quad n_z = \lceil n / n_{\max} \rceil. \quad (3)$$

We denote D as the distance from the antenna array to the output metasurface layer. For simplicity, we assume that the distance between adjacent metasurface layers and the distance between the antenna array and the input metasurface layer are uniform, given by $d = D/L$. Consequently, the propagation distance from meta-atom n on layer $(l-1)$ to the corresponding meta-atom n' on layer l is given by

$$d_{n,n'}^l = \sqrt{d_{n,n'}^2 + d^2}, \quad \forall l \in \mathcal{L} \setminus \{1\}. \quad (4)$$

To address the transmission process between transmit antennas and metasurfaces, we define $\mathbf{W}^l \in \mathbb{C}^{N \times N}, l \in \mathcal{L} \setminus \{1\}$ as the transmission coefficient matrix between layers $(l-1)$ and l , and $\mathbf{W}^1 \in \mathbb{C}^{N \times M}, l \in \mathcal{L} \setminus \{1\}$ as transmission coefficient matrix between the transmit antenna and the first metasurface layer of the SIM. According to the Rayleigh-

Sommerfeld diffraction theory [38], the (n, n') -th entry of \mathbf{W} is given by

$$w_{n,n'}^l = \frac{A_t d}{(d_{n,n'}^l)^2} \left(\frac{1}{2\pi d_{n,n'}^l} - j \frac{1}{\lambda} \right) e^{j2\pi d_{n,n'}^l \lambda}, l \in \mathcal{L} \setminus \{1\} \quad (5)$$

where A_t is the area of each meta-atom in the SIM, and λ is the wavelength. Similarly, the (k, n) -th entry $w_{k,n}$ of \mathbf{W}^1 is obtained by replacing $d_{n,n'}^l$ in (5) with $d_{k,n}^1$, respectively, where the distance from antenna element k to meta-atom n at the first metasurface is given by [23]:

$$d_{k,n}^1 = \left[\left(\left(n_z - \frac{n_{\max} + 1}{2} \right) d_a - \frac{\lambda}{2} \left(k - \frac{K + 1}{2} \right) \right)^2 + \left(n_x - \frac{n_{\max} + 1}{2} \right)^2 d_a^2 + d^2 \right]^{1/2}. \quad (6)$$

The transfer function \mathbf{G} of the SIM is then given by [28]:

$$\mathbf{G} = \Phi^L \mathbf{W}^L \Phi^{L-1} \dots \Phi^2 \mathbf{W}^2 \Phi^1 \in \mathbb{C}^{N \times N}. \quad (7)$$

B. Channel Model

For the wireless channels, we consider a quasi-static flat-fading model. Let \mathbf{h}_m and $\mathbf{h}_e \in \mathbb{C}^{1 \times N}$ denote the channels between BS and CU m , and between BS and Eve, respectively. The channel spanning from the output metasurface to CU/Eve m , which is modeled according to a Rician fading channel model, can be expressed as

$$\mathbf{h}_\varepsilon = \sqrt{\frac{\beta_\varepsilon}{1 + \kappa}} \left(\sqrt{\kappa} \mathbf{h}_\varepsilon^{\text{LoS}} + \mathbf{h}_\varepsilon^{\text{NLoS}} \right) \in \mathbb{C}^{1 \times N} \quad (8)$$

where $\varepsilon \in \{m, e\}$ and κ is the Rician factor; $\beta_\varepsilon = C_0 d_\varepsilon^{-\alpha}$ is the distance-dependent path loss, with C_0 and d_ε being the path loss at a reference distance of 1 meter and the distance from the output metasurface to CU/Eve m , respectively, and α being the path loss exponent; $\mathbf{h}_\varepsilon^{\text{LoS}}$ and $\mathbf{h}_\varepsilon^{\text{NLoS}} \in \mathbb{C}^{1 \times N}$ denote the line-of-sight (LoS) and non-LoS (NLoS) components of the channel from the output metasurface to CU/Eve m , respectively. Similar to [29] and [39], we adopt a spatially correlated channel model to represent the NLoS component of the channel \mathbf{h}_ε , i.e., $\mathbf{h}_\varepsilon^{\text{NLoS}} \sim \mathcal{CN}(0, \mathbf{R})$ where $\mathbf{R} \in \mathbb{C}^{N \times N}$ is the spatial correlation among the channels associated with different meta-atoms on the last layer. By considering far-field wave propagation in an isotropic scattering wireless environment, the (n, n') -th entry of \mathbf{R} can be expressed as

$$\mathbf{R}_{n,n'} = \text{sinc}(2d_{n,n'} / \lambda) \quad (9)$$

where $\text{sinc}(\tau) = \sin(\pi\tau) / (\pi\tau)$ is the normalized sinc function.

Let $\psi_\varepsilon^a \in [0, 2\pi)$ and $\psi_\varepsilon^e \in [0, \pi/2]$ represent the physical azimuth and elevation angles of CU/Eve m , respectively. The LoS component $\mathbf{h}_\varepsilon^{\text{LoS}}$ of channel \mathbf{h}_ε can be then modelled as [39]

$$\mathbf{h}_\varepsilon^{\text{LoS}} = \mathbf{a}_N(\psi_\varepsilon^a, \psi_\varepsilon^e) \quad (10)$$

wherein the n -th entry is given by

$$[\mathbf{a}_N(\psi_\varepsilon^a, \psi_\varepsilon^e)]_n = \exp \left\{ \frac{j2\pi d_a}{\lambda} \left(n_x \sin \psi_\varepsilon^a \sin \psi_\varepsilon^e + n_z \cos \psi_\varepsilon^e \right) \right\}.$$

To design an effective beamforming scheme and allocate system resources efficiently, accurate and complete CSI is essential. For legitimate CUs, CSI can typically be obtained

using standard channel estimation algorithms. However, due to Eve's tendency to conceal its presence, the CSI for this entity is often uncertain. In this paper, we assume that the channel between the output metasurface and Eve is imperfect, which can be modeled as [40], [41]:

$$\hat{\mathbf{h}}_e = \mathbf{h}_e - \Delta \mathbf{h}_e \quad (11)$$

where \mathbf{h}_e denotes the perfect Eve's CSI, and the CSI error vector is assumed to follow the circularly symmetric complex gaussian distribution, i.e., $\Delta \mathbf{h}_e \sim \mathcal{CN}(\mathbf{0}, \delta_e^2 \mathbf{I})$ with δ_e being the error variance.

Let $\mathbf{s} \triangleq [s_1, \dots, s_M]^\top \in \mathbb{C}^M$ be the transmit signal vector, with s_m being the symbol information for CU m with $\mathbb{E}[\mathbf{s}^H \mathbf{s}] = \mathbf{I}$. We denote by $\mathbf{p} \triangleq [p_1, \dots, p_M]^\top \in \mathbb{C}^M$ the transmit power vector, where p_m the power allocation for CU m . Accordingly, the received signal at CU m is expressed as

$$y_m = \underbrace{\mathbf{h}_m^H \mathbf{G} \mathbf{w}_m^1 \sqrt{p_m} s_m}_{\text{Desired Signal}} + \underbrace{\sum_{j=1, j \neq m}^M \mathbf{h}_m^H \mathbf{G} \mathbf{w}_j^1 \sqrt{p_j} s_j + n_m, \forall m \in \mathcal{M}}_{\text{Inter-user Interference}} \quad (12)$$

where $n_m \sim \mathcal{CN}(0, \sigma_m^2)$ is the additive white Gaussian noise (AWGN) with mean zero and variance σ_m^2 . The communication signal-to-interference-plus-noise ratio (SINR) at CU m then can be expressed as:

$$\gamma_m = \frac{|\mathbf{h}_m^H \mathbf{G} \mathbf{w}_m^1|^2 p_m}{\sum_{j=0, j \neq m}^M |\mathbf{h}_m^H \mathbf{G} \mathbf{w}_j^1|^2 p_j + \sigma_m^2}, \quad \forall m \in \mathcal{M}. \quad (13)$$

Due to the uncertainty in Eve's CSI, the received signal at Eve can be expressed as follows:

$$y_e = (\hat{\mathbf{h}}_e^H + \Delta \mathbf{h}_e^H) \mathbf{G} \mathbf{w}_m^1 \sqrt{p_m} s_m + \sum_{j=1, j \neq m}^M (\hat{\mathbf{h}}_e^H + \Delta \mathbf{h}_e^H) \mathbf{G} \mathbf{w}_j^1 \sqrt{p_j} s_j + n_e \quad (14)$$

where $n_e \sim \mathcal{CN}(0, \sigma_e^2)$ is the AWGN with mean zero and variance σ_e^2 . Under the assumption of imperfect Eve's CSI, the CSI error component $\Delta \mathbf{h}_e$ is treated as a source of interference. Accordingly, the achievable SINR for the signal s_m at Eve is given by

$$\hat{\gamma}_e^m = \frac{|\hat{\mathbf{h}}_e^H \mathbf{G} \mathbf{w}_m^1|^2 p_m}{\Psi_m} \quad (15)$$

where $\Psi_m \triangleq |\Delta \mathbf{h}_e^H \mathbf{G} \mathbf{w}_m^1|^2 p_m + \sum_{j=0, j \neq m}^M |(\hat{\mathbf{h}}_e^H + \Delta \mathbf{h}_e^H) \mathbf{G} \mathbf{w}_j^1|^2 p_j + \sigma_e^2$.

To evaluate the security performance of the system, we adopt the achievable secrecy rate as the primary performance metric, defined as:

$$R_m(\mathbf{p}, \boldsymbol{\theta}) = \left[\log_2(1 + \gamma_m) - \log_2(1 + \hat{\gamma}_e^m) \right]^+ \quad (16)$$

where $[x]^+ = \max(x, 0)$.

C. Problem Formulation

Finally, we formulate the joint optimization of SIM-based wave-domain beamforming and BS transmit power allocation as a secrecy-rate maximization problem. The objective is to maximize the average secrecy rate ASR across all users, $\bar{R}(\mathbf{p}, \boldsymbol{\theta})$, which is given by

$$(\mathcal{P}_1) : \max_{\mathbf{p}, \boldsymbol{\theta}} \bar{R}(\mathbf{p}, \boldsymbol{\theta}) \triangleq \frac{1}{M} \sum_{m=1}^M R_m(\mathbf{p}, \boldsymbol{\theta}) \quad (17a)$$

$$\text{s.t.} \quad \sum_{m=1}^M p_m \leq P_0 \quad (17b)$$

$$\log_2(1 + \gamma_m) \geq R_{\min}, \quad \forall m \in \mathcal{M} \quad (17c)$$

$$\theta_n^l \in [0, 2\pi], \quad \forall n \in \mathcal{N}, l \in \mathcal{L} \quad (17d)$$

where $\boldsymbol{\theta} \triangleq [(\boldsymbol{\theta}^1)^\top, (\boldsymbol{\theta}^2)^\top, \dots, (\boldsymbol{\theta}^L)^\top]^\top$ with $\boldsymbol{\theta}^l \triangleq [\theta_1^l, \theta_2^l, \dots, \theta_N^l]^\top$, R_{\min} is the required minimum data rate and P_0 is the transmit power budget at BS. Here, (17b) ensures that the total allocated power do not exceed the power budget P_0 ; (17c) guarantees the satisfaction of minimum data rate R_{\min} for all CUs $m \in \mathcal{M}$; and (17d) imposes that the phase shift θ_n^l must take a continuous value in range $[0, 2\pi]$.

Note that due to the strong coupling between the transmit power vector \mathbf{p} and the SIM phase-shift vector $\boldsymbol{\theta}$, as well as the continuous phase constraints on each meta-atom, problem (\mathcal{P}_1) is inherently non-convex. In addition, the large number of meta-atoms in the SIM architecture results in an extremely high-dimensional design space, which makes the practical solution of problem (\mathcal{P}_1) particularly challenging. Conventional one-shot optimization methods must be repeatedly executed at every time slot, leading to prohibitively high computational complexity and substantial processing overhead.

Although DRL provides a promising alternative, classical DRL approaches often suffer from poor scalability and slow convergence when applied to such high-dimensional and strongly coupled SIM configuration problems. To address these challenges, this paper proposes a novel QRL algorithm that efficiently approximates the optimal policy with significantly faster convergence than conventional DRL methods. Before presenting the proposed quantum learning framework, we reformulate the original deterministic optimization problem into a stochastic optimization problem to capture the time-varying and uncertain nature of the wireless environment.

D. Stochastic Optimization Problem Formulation

In practical wireless environments, channel conditions and the eavesdropper's CSI vary over time and are inherently uncertain. Solving problem (\mathcal{P}_1) in a deterministic one-shot manner would require repeated re-optimization under complete channel knowledge, which is computationally prohibitive and unrealistic. Therefore, we reformulate the problem as a stochastic sequential decision-making problem to capture environmental dynamics and enable adaptive long-term secrecy optimization.

The joint SIM configuration and power allocation problem is formulated as a sequential decision-making process and modeled within a reinforcement learning framework, represented by the tuple $\langle \mathcal{S}, \mathcal{A}, \mathcal{R} \rangle$, where \mathcal{S} , \mathcal{A} , and \mathcal{R} denote the state space, action space, and reward function, respectively.

State space: The state space characterizes the observable environmental information that evolves over time. In the considered system, the CSI of legitimate users can be accurately obtained at the end of each time slot. However, as discussed in Section II, acquiring perfect CSI of the eavesdropper is generally infeasible. Accordingly, the state observed at time slot t is defined as

$$\mathbf{s}_t = \{\mathbf{h}_m^t, \hat{\mathbf{h}}_e^t\}_{m \in \mathcal{M}} \quad (18)$$

where \mathbf{h}_m^t is the perfect CSI of CU m and $\hat{\mathbf{h}}_e^t$ denotes the imperfect CSI of eavesdropper.

Action space: The action space consists of the control decisions selected by the agent at each time slot, including transmit power allocation and SIM phase-shift configuration, and is defined as

$$\mathbf{a}_t = \{\mathbf{p}_t, \boldsymbol{\theta}_t\}. \quad (19)$$

These actions directly determine the SIM wave-domain beamforming behavior and the BS resource allocation strategy. The agent's decisions must satisfy the total transmit power constraint (17b) and the SIM phase-shift constraint (17d). Since meta-atoms operate independently, constraint (17d) is enforced by restricting $\boldsymbol{\theta}_t$ within the action space. To satisfy the power constraint, the transmit power vector \mathbf{p}_t is normalized such that $\sum_{m=1}^M p_m = P_0$, following [42].

Reward: Following problem (\mathcal{P}_1) , the agent is designed to maximize the long-term ASR while satisfying the transmit power and QoS constraints in (17b)–(17d). Since the action design and output normalization explicitly enforce constraints (17b) and (17d), reward design only needs to consider constraint (17c). Consequently, the instantaneous reward at time slot t is therefore defined as

$$r_t = \begin{cases} \bar{R}(\mathbf{p}, \boldsymbol{\theta}), & \text{if (17c) are satisfied,} \\ 0, & \text{otherwise} \end{cases} \quad (20)$$

which encourages the agent to learn policies that achieve high secrecy performance while maintaining feasible system operation.

III. QUANTUM REINFORCEMENT LEARNING-BASED SOLUTION

A. Preliminaries of Reinforcement Learning

To address the stochastic optimization problem formulated in Section II-D, a variety of classical DRL algorithms, including DDPG [43], TD3 [44], and PPO [45], can be employed. Among these methods, PPO has recently attracted significant attention due to its favorable scalability, stable learning behavior, and robustness in high-dimensional continuous control tasks. PPO adopts an actor-critic architecture, in which the actor network generates actions according to a stochastic policy $\pi_{\theta_a}(\mathbf{a}_t | \mathbf{s}_t)$ based on the observed state \mathbf{s}_t , while the critic network evaluates the expected long-term performance of the current policy and provides gradient-based feedback to guide policy updates. A key feature that distinguishes PPO from other policy-gradient algorithms is its clipped surrogate objective function, which explicitly constrains excessive deviations between successive policy updates. This mechanism

effectively balances policy improvement and training stability, thereby mitigating destructive updates that may otherwise arise in high-dimensional optimization problems.

Within the PPO framework, the critic network estimates the state-value function $V(s_t)$, which quantifies the expected discounted cumulative reward achievable from state s_t . It is mathematically expressed as

$$V(s_t) = \mathbb{E} \left[\sum_{i=0}^{\infty} \gamma^i r_{t+i} \right] \quad (21)$$

where $\gamma \in [0, 1]$ denotes the discount factor that controls the relative importance of future rewards, and r_{t+i} represents the instantaneous reward defined in (20). To further reduce the variance of policy-gradient estimates while maintaining low bias, PPO incorporates the GAE technique to approximate the advantage function. The GAE is given by

$$\hat{A}(s_t) = \sum_{i=0}^{\infty} (\gamma\omega)^i (r_{t+i} + \gamma V(s_{t+i+1}) - V(s_{t+i})) \quad (22)$$

where $\omega \in [0, 1]$ is the GAE smoothing coefficient that governs the bias-variance tradeoff in advantage estimation by weighting multi-step temporal-difference errors over different horizons.

To maintain training stability and prevent excessively large policy updates, PPO employs a clipping mechanism that explicitly constrains the deviation between the updated policy and the previous policy. While the learning rate uniformly scales the size of updates, the clipping operation enforces a trust region around the old policy, ensuring that policy updates remain within a controlled range. Specifically, the probability ratio between the current and previous policies is restricted within the interval $[1 - \epsilon, 1 + \epsilon]$, which can be expressed as

$$\text{clip}(\psi, 1 - \epsilon, 1 + \epsilon) = \begin{cases} 1 + \epsilon, & \text{if } \psi > 1 + \epsilon \\ \psi, & \text{if } 1 - \epsilon \leq \psi \leq 1 + \epsilon \\ 1 - \epsilon, & \text{if } \psi < 1 - \epsilon \end{cases} \quad (23a)$$

$$\text{clip}(\psi, 1 - \epsilon, 1 + \epsilon) = \begin{cases} 1 + \epsilon, & \text{if } \psi > 1 + \epsilon \\ \psi, & \text{if } 1 - \epsilon \leq \psi \leq 1 + \epsilon \\ 1 - \epsilon, & \text{if } \psi < 1 - \epsilon \end{cases} \quad (23b)$$

$$\text{clip}(\psi, 1 - \epsilon, 1 + \epsilon) = \begin{cases} 1 + \epsilon, & \text{if } \psi > 1 + \epsilon \\ \psi, & \text{if } 1 - \epsilon \leq \psi \leq 1 + \epsilon \\ 1 - \epsilon, & \text{if } \psi < 1 - \epsilon \end{cases} \quad (23c)$$

where ϵ is the limit adjustment parameter. Based on this operator, the clipped surrogate objective is given by

$$L(\theta_a) = \mathbb{E}_t \left[\hat{A}(s_t, a_t) \min \left(p_t(\theta_a), \text{clip}(p_t(\theta_a), 1 - \epsilon, 1 + \epsilon) \right) \right] \quad (24)$$

where $p_t(\theta_a) = \pi_{\theta_a^{\text{new}}}(\mathbf{a}_t | \mathbf{s}_t) / \pi_{\theta_a^{\text{old}}}(\mathbf{a}_t | \mathbf{s}_t)$ is the likelihood ratio between the new and old policies. Subsequently, the overall loss function is formulated as a combination of the clipped surrogate objective, a value function error term, and an entropy bonus to ensure sufficient exploration, as originally proposed in [45], and is defined as

$$\mathcal{L} = \mathcal{L}^{\text{CLIP}}(\theta_a) - c_1 K(\pi_{\theta_a}) + c_2 \mathcal{L}^{VF}(\theta_c) \quad (25)$$

where c_1 and c_2 are the entropy and value loss coefficients, respectively. $K(\pi_{\theta_a}) = \mathbb{E}_t \left[-\sum_a \pi_{\theta_a}(a | s) \log \pi_{\theta_a}(a | s) \right]$ is an entropy bonus and $\mathcal{L}^{VF}(\theta_c) = \mathbb{E}_t \left[(R_t - V_{\theta_c}(s_t))^2 \right]$ is a squared-error loss. The critic network is trained by minimizing the mean-squared temporal-difference error

$$L(\theta_c) = \mathbb{E}_t \left[r_{t+i} + \gamma V(s_{t+i+1}) - V(s_{t+i}) \right]. \quad (26)$$

Although PPO exhibits strong performance in many complex control tasks, its conservative update mechanism can

Algorithm 1 Proposed Q-PPO Algorithm for Solving (17)

1: **Input:** Maximum interaction steps, batch size, number of epochs K , mini-batch size, discount factor γ , GAE parameter λ , clipping threshold ϵ .
2: **Initialization:** Hybrid quantum-classical actor network π_{θ_a} and classical critic network V_{θ_c} .
3: Determine the number of sampling iterations $M = \frac{\text{max interaction steps}}{\text{batch size}}$.
4: **for** $m = 1$ to M **do**
5: Collect batch size trajectories using policy π_{θ_a} ;
6: **for** each step t **do**
7: Interact with environment, record $(\mathbf{s}_t, \mathbf{a}_t, r_t, s_{t+1}, \text{done})$;
8: **end for**
9: Compute state-value function $V(s_t) = \mathbb{E} \left[\sum_{i=0}^{\infty} \gamma^i r_{t+i} \right]$;
10: Compute GAE:

$$\hat{A}(s_t) = \sum_{i=0}^{\infty} (\gamma\omega)^i (r_{t+i} + \gamma V(s_{t+i+1}) - V(s_{t+i}))$$
;
11: Store trajectories, returns, and advantages in buffer
12: **for** $k = 1$ to K **do**
13: Shuffle buffer and divide into mini-batches;
14: **for** each mini-batch **do**
15: Extract mini batch data: states, actions, returns, advantages;
16: Compute policy ratio $p_t(\theta_a) = \frac{\pi_{\theta_a^{\text{new}}}(\mathbf{a}_t | \mathbf{s}_t)}{\pi_{\theta_a^{\text{old}}}(\mathbf{a}_t | \mathbf{s}_t)}$;
17: Compute clipped objective:

$$\mathcal{L}^{\text{CLIP}}(\theta_a) = \mathbb{E}_t \left[\min \left(r_{\theta_a}(t) \hat{A}_t, \text{clip}(r_{\theta_a}(t), 1 - \epsilon, 1 + \epsilon) \hat{A}_t \right) \right]$$
;
18: Compute value loss: $\mathcal{L}^{VF}(\theta_c) = \mathbb{E}_t \left[(R_t - V_{\theta_c}(s_t))^2 \right]$;
19: Compute entropy bonus $K(\pi_{\theta_a}) = \mathbb{E}_t \left[-\sum_a \pi_{\theta_a}(a | s) \log \pi_{\theta_a}(a | s) \right]$;
20: Compute total loss: $\mathcal{L} = \mathcal{L}^{\text{CLIP}}(\theta_a) - c_1 K(\pi_{\theta_a}) + c_2 \mathcal{L}^{VF}(\theta_c)$;
21: Update parameters θ_a and θ_c ;
22: **end for**
23: **end for**
24: **end for**

inadvertently limit exploration of substantially different strategies, which may slow convergence in extremely high-dimensional optimization problems. This limitation becomes particularly pronounced in SIM configuration in (17), where the action space grows rapidly with the number of meta-atoms and layers and the decision variables are strongly coupled. Consequently, classical PPO often requires a large number of training episodes to sufficiently explore the environment. To address this scalability bottleneck, we propose a novel quantum reinforcement learning algorithm, termed Q-PPO, which is designed to approximate the optimal policy with significantly faster convergence than conventional DRL methods.

B. Proposed Q-PPO Algorithm

Building upon the classical PPO framework, the proposed Q-PPO algorithm preserves the standard training pipeline while enhancing the policy representation through the integration of a PQC into the actor network. Specifically, both classical PPO and Q-PPO follow the same overall procedural framework, as summarized in Algorithm 1 and visually illustrated in Fig. 2. At the beginning of training, a vectorized simulation environment is constructed and reset to generate initial states. The actor-critic networks, together with their corresponding parameters and optimizers, are then initialized. Replay buffers are allocated to store observed states, actions, and rewards. During each training iteration, the agent interacts with the environment to collect transition data, after which returns and advantages are computed based on the recorded rewards, estimated state values, and termination signals. The actor and critic parameters are subsequently updated by minimizing the objective functions in (24) and (26), respectively, through an

optimizer.

Although both algorithms share the same training procedure and optimization routine, they differ fundamentally in their policy representations. Classical PPO parameterizes the actor using a DNN, whereas Q-PPO replaces the DNN with a PQC, thereby enabling quantum-enhanced policy learning. As shown in Fig. 2, this modification is confined to the actor block, while the critic network remains fully classical, following the framework introduced in [46]. Consequently, the principal distinction between classical PPO and Q-PPO lies in the actor’s policy model. Furthermore, following the hybrid design philosophy in [35], and to address the extremely high dimensionality of SIM configuration as well as the limited scalability of current quantum hardware, we adopt a hybrid quantum-classical architecture that integrates pre-encoding neural networks, PQCs, and post-processing neural networks. In this design, PQC is responsible for learning compact and expressive policy representations, while lightweight classical modules handle large-scale state and action mappings. This hybrid structure effectively balances representational power, learning efficiency, and hardware feasibility. Therefore, the proposed hybrid quantum-classical Q-PPO framework generally maintains the standard training procedure while introducing a strongly quantum-enhanced policy representation even with limited quantum hardware. Before presenting the detailed PQC architecture, we next provide an overview of how quantum mechanisms enhance the learning process of DRL agents.

1) Quantum Computing-enhanced Reinforcement Learning

In quantum computing, the basic units of information are represented by the computational basis states of a single quantum bit (qubit) $|0\rangle = [1, 0]^\top$ and $|1\rangle = [0, 1]^\top$, corresponding to the 0 and 1 states of a classical bit. However, a crucial distinction is that a qubit can exist in a state of quantum superposition. The system comprising q qubits spans a 2^q -dimensional Hilbert space $\mathcal{H} = (\mathbb{C}^2)^{\otimes q}$, allowing a general quantum state to be represented as a linear combination of the computational basis states:

$$|\psi\rangle = \sum_{\alpha_i=0}^{2^q-1} c_i |\alpha_i\rangle \quad (27)$$

where c_i is complex coefficient representing the occurrence of $|\alpha_i\rangle$, and according to the probability conservation property of quantum dynamics $\sum_{i=0}^{2^q-1} |c_i|^2 = 1$. When applied in computation, quantum states represent inputs in a simultaneous case and thus allow quantum circuits to evaluate multiple inputs. In the context of DRL, this capability allows quantum-enhanced agents to process multiple state-action pairs [33] through appropriate qubit transformations.

These qubit transformations are implemented through quantum operators U , referred to as quantum gates, acting on the Hilbert space of the quantum system. Mathematically, the state evolution under a quantum gate is expressed as

$$|\psi'\rangle = U|\psi\rangle = \sum_{\alpha_i=0}^{2^q-1} c_i U|\alpha_i\rangle. \quad (28)$$

In a closed quantum system, all admissible transformations must be reversible and are therefore represented by unitary matrices that satisfy $UU^\top = U^\top U = I$. A PQC consists

of a sequence of such unitary gates with tunable parameters, which together define a trainable quantum model. The PQC with q qubits covers a $(2\log_2 Q)$ -dimension Hilbert space and covers all Q classical parameters. This allows PQC to reduce the number of required parameters to $\mathcal{O}(\text{poly}(q))$ compared to the Q parameters of a classical NN network [47]. The representative example of this quantum advantage is Grover’s search algorithm [48], which identifies a marked item in a search space with only $\mathcal{O}(\sqrt{2^q})$ queries, significantly outperforming the classical $\mathcal{O}(2^Q)$ complexity of classical search. Consequently, encoding operational states and actions into quantum states substantially reduces the dimensionality of the decision space [49]. Particularly in the context of the high-dimensional SIM decision-making problem (\mathcal{P}_1), this capability allows for improved training efficiency of quantum-enhanced DRL agents. We also note that the agent in the proposed quantum DRL framework can be trained on classical computers, enhancing practicality in the context of limited quantum hardware resources. Next, we present the PQC architecture in detail.

2) Parameterized Quantum Circuit

In this work, we adopt a widely used hardware-efficient ansatz-based PQC [50]. This architecture primarily employs single-qubit Pauli rotation gates and two-qubit entangling gates to construct expressive yet shallow quantum circuits suitable for near-term quantum devices. Specifically, we utilize the Pauli- Y and Pauli- Z operators, whose matrix representations are given by:

$$Y = \begin{bmatrix} 0 & -i \\ i & 0 \end{bmatrix}; \quad Z = \begin{bmatrix} 1 & 0 \\ 0 & -1 \end{bmatrix} \quad (29)$$

where $i = \sqrt{-1}$. These operators enable rotations of a qubit around the corresponding Bloch sphere axes, thereby controlling both the amplitude and phase of the quantum state. Denote φ the rotation angle, the associated parameterized single-qubit rotation gates are defined as

$$R_Y(\varphi) = \exp(-i\varphi Y/2); \quad R_Z(\varphi) = \exp(-i\varphi Z/2). \quad (30)$$

To introduce quantum entanglement between qubits, we further employ the two-qubit controlled- Z (CZ) gate, which is a standard entangling operator in hardware-efficient PQC designs and is represented by

$$CZ = \text{diag}(1, 1, 1, -1). \quad (31)$$

These parameterized rotation and entangling gates together form the fundamental building blocks of the proposed PQC architecture.

As illustrated in Fig. 2, the proposed PQC architecture is composed of η layers, each containing three blocks: an encoding block, a variational block, and an entangling block. The PQC starts from the fixed initial state $|0\rangle^{\otimes q}$, where q denotes the number of qubits. A Hadamard gate (H) is first applied to create a superposition state. Next, the vectorized classical medium states s_t are encoded into quantum states $|s_t\rangle$ suitable for processing within the PQC. This encoding is implemented in the encoding block using $R_Y(v_{i,j,y}, s_i)$ and $R_Z(v_{i,j,z}, s_i)$ rotation gates, where $v_{i,j}$ is the input scaling parameter corresponding to qubit i and layer j , and s_i is the

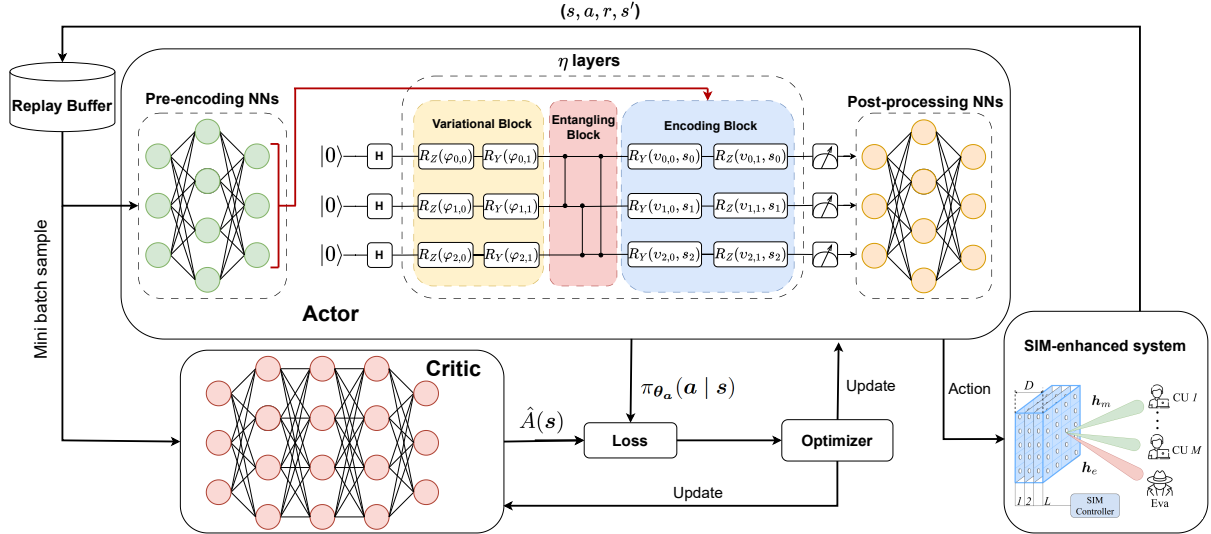


Fig. 2: The proposed hybrid quantum-classical Q-PPO framework.

characteristics of the environment state encoded by qubit i . Since these gates have a periodicity of 2π while the observable space of the classical medium may exceed this range, the classical states are pre-normalized to the interval $[-\pi, \pi]$ by using the input scaling parameters. The encoding unitaries in each PQC layer are then given by

$$U_{\text{enc}} = \bigotimes_{i=0}^{q-1} R_Z(v_{i,j,z}, s_j) R_Y(v_{i,j,y}, s_j). \quad (32)$$

The variational and entangling blocks then act similarly to hidden layers in a neural network, performing cumulative transformations on the quantum states. Specifically, each i -th qubit is rotated by an angle to produce the required values, such as actions or states. In this design, the rotations are performed using $R_Y(\varphi_{i,j,y})$ and $R_Z(\varphi_{i,j,z})$ gates, where $\varphi_{i,j}$ represents the rotation angle of qubit i in layer j . The variational unitaries in each PQC layer are then given by

$$U_{\text{var}} = \bigotimes_{i=0}^{q-1} R_Y(\varphi_{i,j,y}) R_Z(\varphi_{i,j,z}). \quad (33)$$

Each layer then applies a sequence of CZ gates to establish entanglement between neighboring qubits U_{ent} . This process is repeated on η layers based on the data reuploading technique and allows the computation on each qubit to be maximized. The actor PQC unitary map with η layers could be written compactly as

$$U(\theta_a) = \prod_{j=1}^{\eta} U_{\text{ent}} U_{\text{var}}(\varphi) U_{\text{enc}}(\mathbf{v}, \mathbf{s}) \quad (34)$$

where $\theta_a \triangleq (\mathbf{v}, \varphi)$ are trainable parameters.

3) Quantum Measurement

The output of the PQC is obtained through quantum measurements of the qubit. A projection measurement described by a Hermitian operator O is called an observational quantity that defines the basis of the Hilbert space of the quantum

system. The result of the measurement is determined through spectral analysis of the eigenvalues α_m corresponding to the components of the computational basis and the orthogonal projections P_m . According to the Born rule, when a quantum state $|\psi\rangle$ is measured, it produces an outcome α_m and is projected onto the state $P_m|\psi\rangle/\sqrt{p(m)}$. The probability of obtaining this outcome is $p(m) = \langle\psi|P_m|\psi\rangle = \langle P_m\rangle_\psi$. It can be seen that for actor networks, this measurement process is equivalent to performing an action s under policy $\pi_{\theta_a}(a | s)$. Consequently, the quantum policy can be defined as

$$\pi_{\theta_a}(a | s) = \langle P_a \rangle_{s, \theta_a}. \quad (35)$$

The policy defined directly from projective measurements lacks explicit control parameters to regulate the exploration-exploitation tradeoff required in reinforcement learning. In particular, an RL agent must be able to smoothly adjust its behavior between uniform random exploration and preferential action selection during exploitation. To enable such control, we adopt a softmax-based stochastic policy parametrization [51]. The quantum policy is therefore rewritten as

$$\pi_{\theta_a}(a | s) = \frac{e^{\zeta \langle O_a \rangle_{s, \theta_a}}}{\sum_{a'} e^{\zeta \langle O_{a'} \rangle_{s, \theta_a}}} \quad (36)$$

where $\zeta > 0$ is an inverse-temperature parameter that controls the sharpness of the action distribution and hence the exploration-exploitation balance. Larger values of ζ lead to more deterministic (exploitation-oriented) behavior, while smaller values encourage more uniform (exploration-oriented) action sampling. The quantity $\langle O_a \rangle_{s, \theta_a}$ denotes the expectation value of an action-dependent observable and is further generalized by introducing trainable weights $w_{a,i}$, yielding

$$\langle O_a \rangle_{s, \theta_a} = \langle \psi_{s, v, \varphi} | \sum_i w_{a,i} H_{a,i} | \psi_{s, v, \varphi} \rangle \quad (37)$$

where $H_{a,i}$ are Hermitian operators associated with action a and qubit i . The full set of trainable parameters is thus $\theta_a = (\mathbf{v}, \varphi, \mathbf{w})$. Following [51], each $H_{a,i}$ is constructed as a tensor

product of Pauli operators or higher-rank projectors defined on the computational basis.

4) Pre-Encoding and Post-Processing

In the proposed PQC-based actor network, environmental state features are embedded into qubits through parameterized single-qubit rotations, specifically $R_Y(v_{i,j,y}, s_i)$ and $R_Z(v_{i,j,z}, s_i)$, which encode classical state variables into quantum amplitudes and phases. For continuous multi-dimensional control problems, each state feature s_i corresponds to one dimension of the state vector \mathbf{s} and can be mapped to a single qubit. Consequently, the number of required qubits must be at least equal to the dimensionality of the state-action space.

In low-dimensional quantum DRL tasks, such direct encoding into rotation gates is effective [35]. However, for large-scale SIM optimization, the state and action spaces are continuous and high-dimensional, making direct encoding impractical due to limited qubit resources. Moreover, increasing circuit depth improves learning performance only up to a certain threshold [52]. These constraints motivate the integration of classical neural networks to assist PQCs in processing complex state and action spaces.

Classical neural network architectures are constructed by cascading multiple transformation layers, which can be represented as a composition

$$\mathcal{Q} = \mathcal{L}_{b_{\eta-1} \rightarrow b_\eta} \circ \mathcal{L}_{b_{\eta-2} \rightarrow b_{\eta-1}} \circ \cdots \circ \mathcal{L}_{b_0 \rightarrow b_1} \quad (38)$$

where \circ denotes the function composition operator, and η denotes the number of layers and the subscripts indicate the input and output dimensions of each layer. Each layer maps a b -dimensional input to a b' -dimensional output through operations such as linear transformations followed by nonlinear activations, which can be expressed as

$$\mathcal{L}_{n_0 \rightarrow n_1}(\mathbf{x}) = \sigma(\boldsymbol{\theta}\mathbf{x} + \boldsymbol{\rho}) \quad (39)$$

where \mathbf{x} is an input vector of dimension b , $\boldsymbol{\theta}$ is a matrix of size $b' \times b$, and $\boldsymbol{\rho}$ is a vector of size b' , the output of a single layer $\mathcal{L}_{b \rightarrow b'}$.

Leveraging this hierarchical representation capability, the proposed hybrid quantum architecture integrates classical neural networks both before and after the PQC [35]. Specifically, the Pre-NN adopts the efficient dimensionality-reduction strategy in [53], where convolutional layers pre-encode high-dimensional observed states into compact feature representations, which are subsequently mapped to PQC encoding gates through a fully connected layer. This provides a rich yet compact representation compatible with the limited number of available qubits. Similarly, the Post-NN comprises fully connected layers applied to quantum measurement outputs to generate continuous multi-dimensional actions. The Post-NN compensates for the limited expressiveness of shallow PQCs constrained by the number of qubits and enhances the overall representational capacity of the hybrid policy network. Unlike conventional DRL architectures that rely on deep and wide neural networks, the proposed Pre-NN/Post-NN modules employ only a small number of hidden layers and neurons, thereby avoiding excessive classical computational overhead, as further discussed in Section IV.

TABLE I: Simulation Parameters

Parameter	Value	Parameter	Value
M	3	K	4
L	3	N	25
d_a	$\lambda/2$ [21]	λ	10.7mm [29]
A_t	$\lambda^2/4$	κ	-30 dB [29]
R_{\min}	75 m	R_{\max}	100 m
c_1	0.01 [54]	c_2	0.5 [54]

IV. PERFORMANCE EVALUATION

In this section, we evaluate the performance of the proposed Q-PPO algorithm and compare it with several benchmark schemes, including PPO, DDPG, TD3, and a random action selection strategy. The simulation setup and parameter configurations are detailed below.

A. Parameter Settings

We consider a SIM-assisted downlink system, whose system configuration is adopted from [14], [21] and [29]. Specifically, the SIM is integrated into the BS and deployed at a height of $H_b = 10$ m. The distance from the antenna array to the output metasurface is set to $D = 5\lambda$. The BS transmit power is $P_0 = 10$ dBm, while the noise powers at the legitimate users (σ_m^2) and the eavesdropper (σ_e^2) are both set to -104 dBm. Legitimate users are randomly distributed within an annular region centered at the BS, with horizontal distances ranging from R_{\min} to R_{\max} . Accordingly, the distance from the output metasurface to the m -th CU/Eve is calculated as $d_e = \sqrt{H_b^2 + R_e^2}$, where R_e denotes the horizontal distance of the corresponding node. For the channel model, the path loss at a reference distance of 1 m is $C_0 = -35$ dB, and the path loss exponent is $\alpha = 3.5$. The variance of the CSI estimation error is given by $\delta_e^2 = \frac{\delta^2}{N} |\hat{h}_e|^2$ [40], where $\delta = 0.1$ represents the relative level of CSI uncertainty.

The main hyperparameters of the quantum and classical PPO algorithms follow the standard configuration of the PPO implementation in [54], including a learning rate (lr) of 3×10^{-4} , a clipping parameter of 0.2, a batch size of 64, a discount factor of 0.99, and a GAE parameter of 0.95 for the bias-variance trade-off. The classical actor-critic network consists of four hidden layers with 1024 neurons each, employing ReLU activation and the Adam optimizer. In the hybrid classical-quantum architecture, the Pre-NN contains two convolutional layers with 128 neurons and one fully connected layer with 64 neurons, while the Post-NN includes two fully connected layers with 62 and 32 neurons, respectively. The PQC comprises four layers operating on five qubits. As described in Section III-B, both the classical and quantum PPO share the same training process, where weight updates are performed every 1024 steps using the Adam optimizer. To enable sufficient exploration, the environment is updated every 20 steps. The remaining simulation parameters are summarized in Table I.

B. Baselines and Performance Metrics

Baselines: To demonstrate the adaptability of the proposed Q-PPO algorithm and its effectiveness in enhancing SIM-enabled secure communications, we compare its performance with the following baseline schemes:

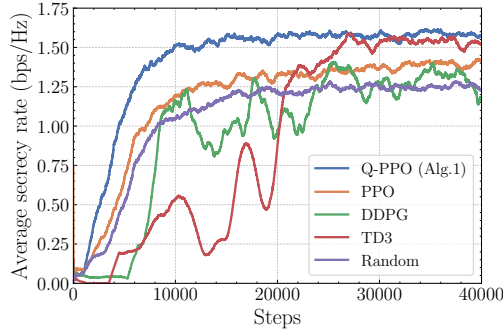


Fig. 3: The convergence of the different algorithms.

- **PPO:** The conventional PPO algorithm [45] is implemented to solve the optimization problem in (17). This baseline serves to isolate and quantify the performance gains achieved by incorporating quantum-enhanced policy representation.
- **TD3 and DDPG:** These baselines are implemented using state-of-the-art DRL algorithms that are widely adopted for continuous control problems [29], [30], providing a fair comparison with established learning-based SIM optimization approaches.
- **Random:** A random configuration scheme is also considered, where the SIM phase shifts are randomly selected within their feasible ranges. This baseline highlights the importance of intelligent SIM control in achieving secure communication performance.

Performance metrics: We evaluate the proposed quantum-DRL-based joint resource allocation and SIM design scheme using two key performance metrics, including the ASR and Jain’s fairness index [55]. The ASR, measured in bits/s/Hz, serves as the optimization objective of problem (\mathcal{P}_1) and reflects the effectiveness of the adopted resource allocation strategy and SIM design:

$$\bar{R}(\mathbf{p}, \boldsymbol{\theta}) = \frac{1}{M} \sum_{m=1}^M R_m(\mathbf{p}, \boldsymbol{\theta}). \quad (40)$$

The higher ASR indicates more efficient utilization of system resources as well as a more effective SIM configuration. To quantify the fairness in resource allocation among the CUs in the system, we employ Jain’s fairness index [55]

$$J = \frac{\left(\sum_{m=1}^M R_m\right)^2}{M \sum_{m=1}^M R_m^2} \quad (41)$$

that provides a bounded measure $J \in [1/M, 1]$, where $1/M$ indicates no fairness and 1 represents perfect fairness.

C. Results and Discussion

1) Convergence Analysis and Impact of Hyper-parameters

We first evaluate the convergence behavior of the different algorithms. As shown in Fig. 3, all algorithms converge steadily toward stable reward values, confirming their effectiveness in solving the optimization problem. As expected, the PPO-based schemes (including the conventional PPO and our proposed Q-PPO algorithm) achieve more stable convergence behavior than that of the other methods. Notably,

the proposed Q-PPO algorithm exhibits superior performance with significantly faster convergence, achieving an optimal ASR of 1.67 bps/Hz, approximately 15% higher than that of the conventional PPO, after more than 20,000 training steps. In contrast, the conventional PPO reaches performance saturation only after nearly 30,000 training steps, indicating that Q-PPO achieves approximately a 30% improvement in convergence speed. Although the advanced TD3 algorithm performs closely to Q-PPO, it similarly requires nearly 30,000 steps to converge. This highlights the effectiveness of the PQC in enhancing the agent’s ability to explore the environment through quantum advantages such as improved state representation and exploration efficiency. Furthermore, comparison with the Random scheme reveals that the SIM phase-shift design improves system security performance by approximately 22%.

Next, we investigate the impact of key hyperparameters of Q-PPO, including learning rate lr , the number of available qubits q , and the number of PQC layers η , as illustrated in Fig. 4. As shown in Fig. 4a, we evaluate different learning rates $lr = (3 \times 10^{-3}, 3 \times 10^{-4}, 3 \times 10^{-6})$. The best performance is achieved at $lr = 3 \times 10^{-4}$, where the algorithm converges faster and achieves higher rewards. This is because a relatively smaller learning rate stabilizes parameter updates and reduces gradient noise, allowing the model to fine-tune its parameters to get a better solution closer to the global optimum. However, when the learning rate is too small (e.g., $lr = 3 \times 10^{-6}$), Q-PPO is not able to escape from the local optima, resulting in slower learning performance. Conversely, a too large learning rate leads to unstable updates and hinders the model’s ability to fine-tune its policy effectively.

As shown in Fig. 4b, we compare training performance on PQC configurations with $q = 3$, $q = 4$, and $q = 5$ qubits. It can be seen that the agent converges to the optimal reward after about 20,000 steps with a PQC of 5 qubits, while the 3- and 4-qubit configurations require about 40,000 and 35,000 steps, respectively. Increasing the number of qubits not only expands the encoding block but also increases the number of measurements that can be performed. This allows PQC to encode richer representations of the classical environment and explore a wider action space at each time slot, thereby improving training.

In Fig. 4c, we vary the number of PQC layers η , considering $\eta = (2, 3, 4)$, and compare the resulting convergence. We can see that the convergence of the algorithm improves as the number of layers increases. The training process in PQC is performed on each layer, similar to NN, where the trainable parameters are tuned to optimize the objective function. In general, adding more layers to the PQC architecture increases the number of trainable parameters and leads to higher computational complexity. However, this allows the computation on each qubit in PQC to be maximized through data reloading between layers, resulting in improved performance.

2) Performance Comparison

Fig. 5a illustrates the ASR versus the number of meta-atoms per layer N . As observed, all evaluated schemes exhibit an increasing secrecy rate when N increases. This trend results from the expanded degrees of freedom, enabling the

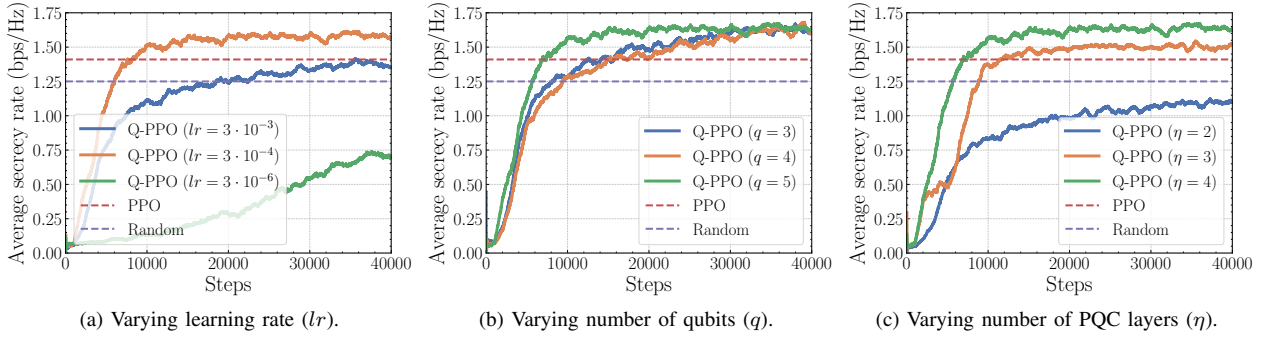


Fig. 4: Comparison of proposed Q-PPO and benchmark schemes (PPO and Random), where we consider varying (a) learning rate lr , (b) number of available qubits q and (c) number of PQC layers η .

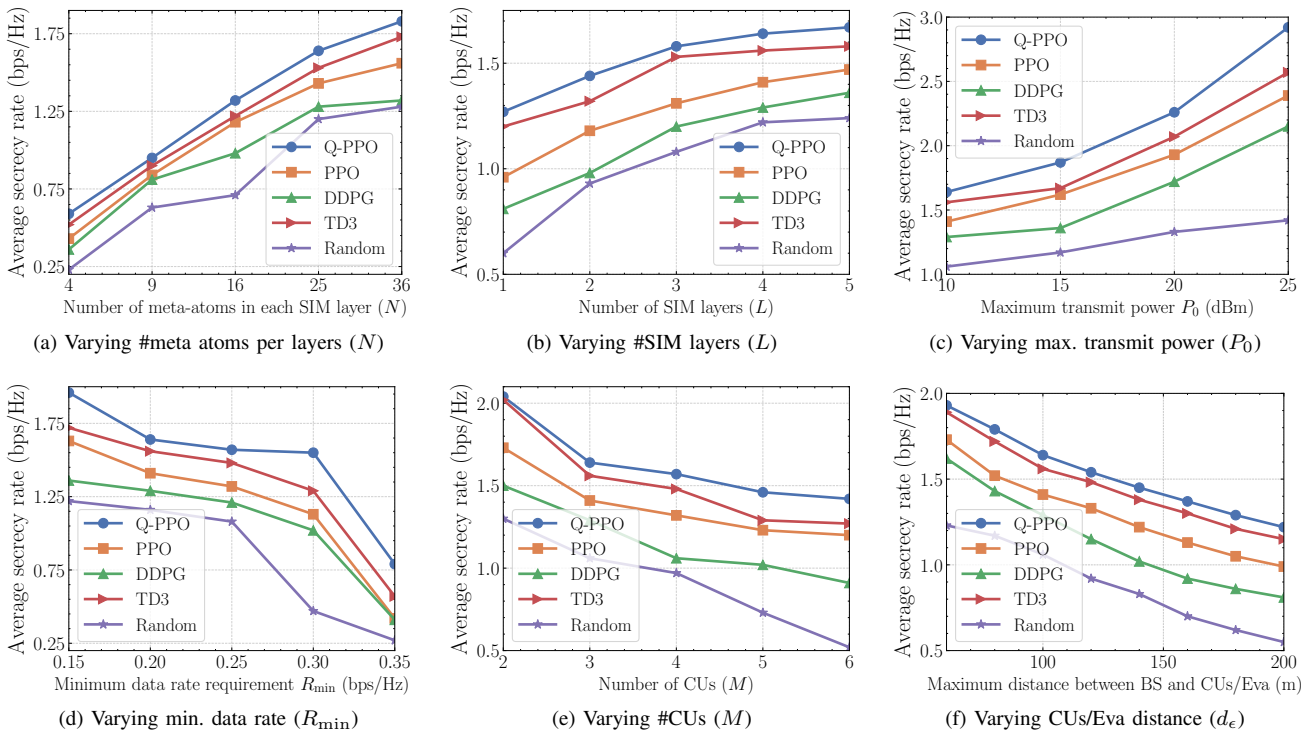


Fig. 5: Evaluation of the average secrecy rate with varying (a) number of meta atoms per layers (N), (b) number of SIM layers (L), (c) maximum transmit power (P_0), (d) minimum data rate requirement (R_{\min}), (e) number of CUs (M), and (f) CUs/Eva distance (d_e).

SIM to be more flexibly tuned for better channel conditions. The proposed Q-PPO algorithm consistently achieves the best performance. When each layer contains relatively few meta-atoms (e.g., $N = 4$ or $N = 9$), PPO and TD3 yield a similar performance to that of Q-PPO due to their lower computational demand. However, as the number of meta-atoms increases, the performance gap becomes more evident, highlighting the PQC-based agent's enhanced ability to represent the environment and facilitate more efficient policy learning.

Fig. 5b shows how the ASR varies with the number of SIM layers L . Increasing L consistently improves secrecy performance for all algorithms, confirming the advantage of multilayer SIM architectures in enhancing signal obfuscation

and enabling more effective physical-layer precoding. Notably, the proposed Q-PPO algorithm achieves comparable security levels with far fewer SIM configurations. For instance, Q-PPO attains an ASR of 1.3 bps/Hz using only one single SIM layer, whereas DDPG requires four layers to achieve a similar performance. However, as the PQC depth increases, the improvement in secrecy rate gradually saturates due to the rapidly growing number of meta-atoms to be optimized, which substantially increases training complexity.

Fig. 5c illustrates the impact of the transmit power budget P_0 on the ASR of the system. As shown, increasing P_0 significantly enhances the ASR. Specifically, for the proposed Q-PPO algorithm, the secrecy rate rises from 1.64 bps/Hz

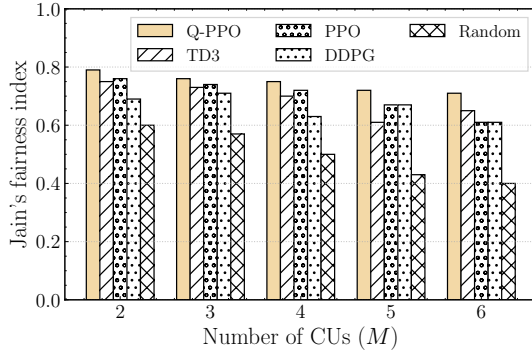


Fig. 6: Jain's index vs. different number of CUs.

to 2.93 bps/Hz when the maximum transmit power increases from 10 to 25 dBm. This improvement arises because a higher transmit power enables the BS to deliver stronger signals to the CUs.

We examine the effect of the minimum data rate requirement R_{\min} on the ASR, as illustrated in Fig. 5d. As R_{\min} increases, tighter QoS constraints lead to a noticeable decline in secrecy performance across all evaluated schemes. In particular, when $R_{\min} = 0.35$ bps/Hz, all schemes experience a sharp degradation, indicating that the system struggles to suppress eavesdropping channels under limited transmit power resources while maintaining the QoS requirements of CUs. Notably, among all compared schemes, the proposed Q-PPO algorithm consistently achieves the highest secrecy rate for various R_{\min} values, demonstrating its strong capability to maintain secure communication even under stringent QoS constraints.

Fig. 5e depicts the ASR as a function of the number of legitimate users M . As M increases, the ASR decreases due to the intensified inter-user interference under a fixed transmit power budget. Notably, SIM-assisted schemes exhibit a significantly slower degradation in secrecy performance compared with their non-SIM counterparts, demonstrating the effectiveness of SIM in mitigating multi-user interference in MISO systems.

Fig. 5f shows the impact of the maximum distance between the BS and the CUs/Eve, denoted by d_{ε} , on the ASR. In this evaluation, the difference $R_{\max} - R_{\min}$ is fixed at 25 m. As the service region moves farther from the BS, the ASR decreases due to increased path loss. Nevertheless, SIM-enabled beamforming maintains consistently higher secrecy rates across all distance ranges, highlighting its robustness against propagation attenuation.

Finally, Fig. 6 compares the fairness index achieved by different algorithms. Since Jain's fairness index is limited by the rate of the user with the poorest channel condition, considering the minimum rate constraint for each user ensures fairness with the index consistently exceeding 0.6. Notably, the proposed Q-PPO algorithm outperforms all other approaches, achieving a fairness level greater than 0.7 even as the number of users increases.

V. CONCLUSIONS

This work investigated SIMs for enhancing physical-layer security in multi-user MISO systems. By enabling multi-stage wave-domain control, SIMs provide substantially higher degrees of freedom than conventional single-layer surfaces, offering an effective mechanism for suppressing multi-user interference and improving secrecy performance in dense wireless environments. To manage the resulting high-dimensional and strongly coupled control problem, we developed a quantum-enhanced reinforcement learning framework that departs from traditional optimization and classical DRL approaches. The proposed Q-PPO algorithm employs a hybrid quantum-classical policy model to overcome scalability limitations and enables adaptive SIM configuration under imperfect channel knowledge. Simulation results demonstrate that SIM-assisted transmission significantly improves secrecy performance and fairness, while Q-PPO achieves faster convergence and stronger adaptability than state-of-the-art DRL baselines. These findings indicate that quantum-enhanced reinforcement learning is a promising paradigm for controlling large-scale programmable metasurface architectures and for enabling secure next-generation wireless networks.

REFERENCES

- [1] L.-H. Hoang, M. H. Pham, Q.-T. Luu, and V.-D. Nguyen, "Secure Multiuser Communications with Stacked Intelligent Metasurfaces Using Quantum Reinforcement Learning," in *Proc. Int. Conf. Adv. Tech. Commun. (ATC), Hanoi, Vietnam, 2025*, pp. 1-6, 2025.
- [2] Z. Zhang, Y. Xiao, Z. Ma, M. Xiao, Z. Ding, X. Lei, G. K. Karagiannidis, and P. Fan, "6G Wireless Networks: Vision, Requirements, Architecture, and Key Technologies," *IEEE Veh. Technol. Mag.*, vol. 14, no. 3, pp. 28-41, 2019.
- [3] N. Yang and A. Shafie, "Terahertz communications for massive connectivity and security in 6G and beyond era," *IEEE Commun. Mag.*, vol. 62, no. 2, pp. 72-78, 2022.
- [4] L. Jin, X. Hu, Y. Lou, Z. Zhong, X. Sun, H. Wang, and J. Wu, "Introduction to wireless endogenous security and safety: Problems, attributes, structures and functions," *China Communications*, vol. 18, no. 9, pp. 88-99, 2021.
- [5] N. Yang, L. Wang, G. Geraci, M. Elkashlan, J. Yuan, and M. Di Renzo, "Safeguarding 5G wireless communication networks using physical layer security," *IEEE Commun. Mag.*, vol. 53, no. 4, pp. 20-27, 2015.
- [6] S. Goel and R. Negi, "Guaranteeing secrecy using artificial noise," *IEEE Trans. Wireless Commun.*, vol. 7, no. 6, pp. 2180-2189, 2008.
- [7] Z. Ren, L. Qiu, J. Xu, and D. W. K. Ng, "Robust Transmit Beamforming for Secure Integrated Sensing and Communication," *IEEE Trans. Commun.*, vol. 71, no. 9, pp. 5549-5564, May 2023.
- [8] H. L. Hung, N. H. Huy, N. C. Luong, Q.-V. Pham, D. Niyato, and N. T. Hoa, "Beamforming Design for Physical Security in Movable Antenna-aided ISAC Systems: A Reinforcement Learning Approach," *IEEE Trans. Veh. Commun.*, pp. 1-5, 2025, Early Access.
- [9] J. Chu, Z. Lu, R. Liu, M. Li, and Q. Liu, "Joint Beamforming and Reflection Design for Secure RIS-ISAC Systems," *IEEE Trans. Veh. Commun.*, vol. 73, no. 3, pp. 4471-4475, 2024.
- [10] L. Dong, H.-M. Wang, and J. Bai, "Active Reconfigurable Intelligent Surface Aided Secure Transmission," *IEEE Trans. Veh. Commun.*, vol. 71, no. 2, pp. 2181-2186, 2022.
- [11] Y. Zhang, S. Zhao, Y. Shen, X. Jiang, and N. Shiratori, "Enhancing the Physical Layer Security of Two-Way Relay Systems With RIS and Beamforming," *IEEE Trans. Inf. Forensics Security*, vol. 19, pp. 5696-5711, 2024.
- [12] C. Jiang, C. Zhang, C. Huang, J. Ge, D. Niyato, and C. Yuen, "RIS-assisted ISAC systems for robust secure transmission with imperfect sense estimation," *IEEE Trans. Wireless Commun.*, 2025.
- [13] H. Guo, Y.-C. Liang, J. Chen, and E. G. Larsson, "Weighted Sum-Rate Maximization for Reconfigurable Intelligent Surface Aided Wireless Networks," *IEEE Trans. Wireless Commun.*, vol. 19, no. 5, pp. 3064-3076, 2020.

[14] J. An, M. D. Renzo, M. Debbah, H. Vincent Poor, and C. Yuen, "Stacked Intelligent Metasurfaces for Multiuser Downlink Beamforming in the Wave Domain," *IEEE Trans. Wireless Commun.*, pp. 1–1, 2025, Early Access.

[15] A. Papazafeiropoulos, J. An, P. Kourtessis, T. Ratnarajah, and S. Chatzinotas, "Achievable rate optimization for stacked intelligent metasurface-assisted holographic MIMO communications," *IEEE Trans. Wireless Commun.*, vol. 23, no. 10, pp. 13 173–13 186, 2024.

[16] N. U. Hassan, J. An, M. Di Renzo, M. Debbah, and C. Yuen, "Efficient beamforming and radiation pattern control using stacked intelligent metasurfaces," *IEEE Open J. Commun. Soc.*, vol. 5, pp. 599–611, 2024.

[17] H. Liu, J. An, X. Jia, L. Gan, G. K. Karagiannidis, B. Clerckx, M. Benni, M. Debbah, and T. J. Cui, "Stacked intelligent metasurfaces for wireless communications: Applications and challenges," *IEEE Wireless Commun.*, vol. 32, no. 4, pp. 46–53, 2025.

[18] J. An, M. Debbah, T. J. Cui, Z. N. Chen, and C. Yuen, "Emerging technologies in intelligent metasurfaces: Shaping the future of wireless communications," *IEEE Trans. Antennas Propag.*, 2025.

[19] H. Niu, J. An, L. Zhang, X. Lei, and C. Yuen, "Enhancing Physical Layer Security for SISO Systems Using Stacked Intelligent Metasurfaces," in *Proc. APWCS*, 2024, pp. 1–5.

[20] H. Niu, X. Lei, J. An, L. Zhang, and C. Yuen, "On the Efficient Design of Stacked Intelligent Metasurfaces for Secure SISO Transmission," in *IEEE Trans. Inf. Forensics Security*, vol. 20, pp. 60–70, Jan. 2025.

[21] M. R. Kavianinia, A. Mohammadi, and V. Meghdadi, "Secrecy Rate Maximization in the Presence of Stacked Intelligent Metasurface," *IEEE Trans. Inf. Forensics Security*, 2025.

[22] J. An, M. Di Renzo, M. Debbah, and C. Yuen, "Stacked Intelligent Metasurfaces for Multiuser Beamforming in the Wave Domain," in *Proc. ICC*, 2023, pp. 2834–2839.

[23] J. An, C. Xu, D. W. K. Ng, G. C. Alexandropoulos, C. Huang, C. Yuen, and L. Hanzo, "Stacked Intelligent Metasurfaces for Efficient Holographic MIMO Communications in 6G," *IEEE J. Sel. Areas Commun.*, vol. 41, no. 8, pp. 2380–2396, Aug. 2023.

[24] X. Yao, J. An, L. Gan, M. Di Renzo, and C. Yuen, "Channel estimation for stacked intelligent metasurface-assisted wireless networks," *IEEE Wireless Commun. Lett.*, vol. 13, no. 5, pp. 1349–1353, 2024.

[25] J. An, A. Chaaban *et al.*, "Hybrid digital-wave domain channel estimator for stacked intelligent metasurface enabled multi-user MISO systems," in *Proc. WCNC*. IEEE, 2024, pp. 1–6.

[26] G. Huang, J. An, Z. Yang, L. Gan, M. Benni, and M. Debbah, "Stacked intelligent metasurfaces for task-oriented semantic communications," *IEEE Wireless Commun. Lett.*, 2024.

[27] J. Li, D. Mengu, N. T. Yardimci, Y. Luo, X. Li, M. Veli, Y. Rivenson, M. Jarrahi, and A. Ozcan, "Spectrally encoded single-pixel machine vision using diffractive networks," *Science Advances*, vol. 7, no. 13, p. eabd7690, 2021.

[28] M.-D. Nguyen, Q. V. Do, Z. Yang, Q.-V. Pham, and W.-J. Hwang, "Distortion Resilience for Goal-Oriented Semantic Communication," *IEEE Trans. Mobile Comput.*, vol. 24, no. 5, pp. 3489–3501, May 2025.

[29] H. Liu, J. An, G. C. Alexandropoulos, D. W. K. Ng, C. Yuen, and L. Gan, "Multi-User MISO with Stacked Intelligent Metasurfaces: A DRL-Based Sum-Rate Optimization Approach," *IEEE Trans. Cogn. Commun. Netw.*, pp. 1–1, 2025, Early Access.

[30] X. Yang, J. Zhang, E. Shi, Z. Liu, J. Liu, K. Zheng, and B. Ai, "Joint SIM Configuration and Power Allocation for Stacked Intelligent Metasurface-assisted MU-MISO Systems with TD3," 2024. [Online]. Available: <https://arxiv.org/abs/2408.05756>

[31] D. T. Hoang, N. Van Huynh, D. N. Nguyen, E. Hossain, and D. Niyato, *Deep Reinforcement Learning for Wireless Communications and Networking: Theory, Applications and Implementation*. John Wiley & Sons, 2023.

[32] C.-Y. Liu, C.-H. A. Lin, C.-H. H. Yang, K.-C. Chen, and M.-H. Hsieh, "Qtrl: Toward practical quantum reinforcement learning via quantum-train," in *Proc. QCE*, vol. 2. IEEE, 2024, pp. 317–322.

[33] K. Cherukuri, A. Lala, and Y. Yardi, "Q-policy: Quantum-enhanced policy evaluation for scalable reinforcement learning," 2025. [Online]. Available: <https://arxiv.org/abs/2505.11862>

[34] S. Y.-C. Chen, "An Introduction to Quantum Reinforcement Learning (QRL)," in *Proc. ICTC*. IEEE, 2024, pp. 1139–1144.

[35] Y.-X. Jin, Z.-W. Wang, H.-Z. Xu, W.-F. Zhuang, M.-J. Hu, and D. E. Liu, "PPO-Q: Proximal Policy Optimization with Parametrized Quantum Policies or Values," 2025. [Online]. Available: <https://arxiv.org/abs/2501.07085>

[36] C. Liu, Q. Ma, Z. J. Luo, Q. R. Hong, Q. Xiao, H. C. Zhang, L. Miao, W. M. Yu, Q. Cheng, L. Li, and T. J. Cui, "A programmable diffractive deep neural network based on a digital-coding metasurface array," *Nature Electronics*, vol. 5, no. 2, pp. 113–122, Feb. 2022.

[37] T. J. Cui, M. Q. Qi, X. Wan, J. Zhao, and Q. Cheng, "Coding metamaterials, digital metamaterials and programmable metamaterials," *Light: Science & Applications*, vol. 3, no. 10, p. e218, Oct. 2014.

[38] X. Lin, Y. Rivenson, N. T. Yardimci, M. Veli, Y. Luo, M. Jarrahi, and A. Ozcan, "All-optical machine learning using diffractive deep neural networks," *Science*, vol. 361, no. 6406, pp. 1004–1008, Jul. 2018.

[39] A. Papazafeiropoulos, P. Kourtessis, D. I. Kaklamani, and I. S. Venieris, "Channel Estimation for Stacked Intelligent Metasurfaces in Rician Fading Channels," *IEEE Wireless Commun. Lett.*, vol. 14, no. 5, pp. 1411–1415, Feb. 2025.

[40] M.-M. Zhao, Q. Wu, M.-J. Zhao, and R. Zhang, "Exploiting Amplitude Control in Intelligent Reflecting Surface Aided Wireless Communication With Imperfect CSI," *IEEE Trans. Commun.*, vol. 69, no. 6, pp. 4216–4231, Jun. 2021.

[41] S. Hong, C. Pan, H. Ren, K. Wang, K. K. Chai, and A. Nallanathan, "Robust Transmission Design for Intelligent Reflecting Surface-Aided Secure Communication Systems With Imperfect Cascaded CSI," *IEEE Trans. Wireless Commun.*, vol. 20, no. 4, pp. 2487–2501, Apr. 2021.

[42] C. Huang, Z. Yang, G. C. Alexandropoulos, K. Xiong, L. Wei, C. Yuen, Z. Zhang, and M. Debbah, "Multi-hop RIS-empowered terahertz communications: A DRL-based hybrid beamforming design," *IEEE J. Sel. Areas Commun.*, vol. 39, no. 6, pp. 1663–1677, 2021.

[43] T. P. Lillicrap, J. J. Hunt, A. Pritzel, N. Heess, T. Erez, Y. Tassa, D. Silver, and D. Wierstra, "Continuous Control with Deep Reinforcement Learning," *Proc. ICLR*, 2016.

[44] S. Fujimoto, H. Hoof, and D. Meger, "Addressing function approximation error in actor-critic methods," in *Proc. ICML*, 2018, pp. 1587–1596.

[45] J. Schulman, F. Wolski, P. Dhariwal, A. Radford, and O. Klimov, "Proximal policy optimization algorithms," 2017. [Online]. Available: <https://arxiv.org/abs/1707.06347>

[46] Y. Kwak, W. J. Yun, S. Jung, J.-K. Kim, and J. Kim, "Introduction to quantum reinforcement learning: Theory and pennylane-based implementation," in *Proc. ICTC*. IEEE, 2021, pp. 416–420.

[47] C.-Y. Liu, E.-J. Kuo, C.-H. Abraham Lin, J. Gensun Young, Y.-J. Chang, M.-H. Hsieh, and H.-S. Goan, "Quantum-train: Rethinking hybrid quantum-classical machine learning in the model compression perspective," *Quantum Machine Intelligence*, vol. 7, no. 2, p. 80, 2025.

[48] Z. Qu and H. Sun, "A secure information transmission protocol for healthcare cyber based on quantum image expansion and grover search algorithm," *IEEE Trans. Netw. Sci. Eng.*, vol. 10, no. 5, pp. 2551–2563, 2022.

[49] A. Paul, K. Singh, A. Kaushik, C.-P. Li, O. A. Dobre, M. Di Renzo, and T. Q. Duong, "Quantum-enhanced drl optimization for doa estimation and task offloading in isac systems," *IEEE J. Sel. Areas Commun.*, 2024.

[50] A. Kandala, A. Mezzacapo, K. Temme, M. Takita, M. Brink, J. M. Chow, and J. M. Gambetta, "Hardware-efficient variational quantum eigensolver for small molecules and quantum magnets," *Nature*, vol. 549, no. 7671, pp. 242–246, 2017.

[51] S. Jerbi, C. Gyurik, S. Marshall, H. Briegel, and V. Dunjko, "Parametrized quantum policies for reinforcement learning," *Advances in Neural Information Processing Systems*, vol. 34, pp. 28 362–28 375, 2021.

[52] A. Skolik, S. Jerbi, and V. Dunjko, "Quantum agents in the gym: a variational quantum algorithm for deep q-learning," *Quantum*, vol. 6, p. 720, 2022.

[53] V. Mnih, K. Kavukcuoglu, D. Silver, A. Graves, I. Antonoglou, D. Wierstra, and M. Riedmiller, "Playing atari with deep reinforcement learning," 2013. [Online]. Available: <https://arxiv.org/abs/1312.5602>

[54] A. Raffin, A. Hill, A. Gleave, A. Kanervisto, M. Ernestus, and N. Dormann, "Stable-Baselines3: Reliable Reinforcement Learning Implementations," *Journal of Machine Learning Research*, vol. 22, no. 268, pp. 1–8, 2021.

[55] R. K. Jain, D.-M. W. Chiu, W. R. Hawe *et al.*, "A quantitative measure of fairness and discrimination," *Eastern Research Laboratory, Digital Equipment Corporation, Hudson, MA*, vol. 21, no. 1, pp. 2022–2023, 1984.